PULSE-PHASE-RESOLVED SPECTROSCOPY OF VELA X-1 WITH *SUZAKU*

Chandreyee Maitra[1] and Biswajit Paul
Raman Research Institute, Sadashivnagar, Bangalore 560080, India; cmaitra@rri.res.in, bpaul@rri.res.in

ABSTRACT

We present a detailed pulse-phase-resolved spectral analysis of the persistent high-mass X-ray binary pulsar Vela X-1 observed with *Suzaku* during 2008 June. The pulse profiles exhibit both intensity and energy dependence with multiple peaks at low energies and double peaks at higher energies. The source shows some spectral evolution over the duration of the observation and care has been taken to average over data with minimum spectral variability for the analysis. We model the continuum with a phenomenological partial covering high-energy cutoff model and a more physical partial covering thermal Comptonization model (CompTT) excluding the time ranges having variable hardness ratio and intensity dependence. For both the models, we detect a cyclotron resonant scattering feature (CRSF) and its harmonic at ∼25 keV and ∼50 keV. Both the CRSF fundamental and harmonics parameters are strongly variable over the pulse phase, with the ratio of the two line energies deviating from the classical value of 2. The continuum parameters also show significant variation over the pulse phase and give us some idea about the changing physical conditions that are seen with the changing viewing angle at different pulse phases and obscuration by the accretion stream at some pulse phases.

Key words: pulsars: general – X-rays: binaries – X-rays: individual (Vela X-1)

1. INTRODUCTION

Vela X-1 (4U 0900−40) is an eclipsing and persistently active high-mass X-ray binary system consisting of a massive (23 $M_\odot$; 34 $R_\odot$) B0.5 1b supergiant HD 77581 (Brucato & Kristian 1972; Nagase 1989) and a ∼1.77 $M_\odot$ neutron star (Rawls et al. 2011). It has an orbital period of 8.964 days (van Kerkwijk et al. 1995) with a slightly eccentric orbit ($e \sim 0.1$). Being a closely spaced binary system (Quaintrell et al. 2003), the neutron star is deeply embedded in the strong stellar wind of the companion which has a mass-loss rate in excess of $10^{-7} M_\odot$ yr^{-1} (Nagase et al. 1986; Sako et al. 1999). It is a prototype candidate for accretion via stellar wind, and the typical X-ray luminosity is of the order of ∼4 × 10^{36} erg s^{-1}. It exhibits pulsations with a period ∼283 s. The source is extremely variable undergoing giant flares (where flux increases by a factor of 20), and abrupt off-states, where the source is almost undetectable for several pulse periods (Inoue et al. 1984; Kreykenbohm et al. 2008; Doroshenko et al. 2011).

The structure of the wind and hence the flaring behavior of Vela X-1 was investigated by Fürst et al. (2010) who also found a systematic trend in the change of column density of absorbing matter along the line of sight in different phases of the orbit. The pulse profiles of Vela X-1 show a complex structure with multiple energy-dependent dips. This has been explored before for other sources, for example in GX 1+4 (Galloway et al. 2001), RX J0812.4−3114 (Corbet & Peele 2000), 1A 1118−61 (Devasia et al. 2011a), GX 304−1 (Devasia et al. 2011b) with *RXTE*, KS 1947+300 (Naik et al. 2006) with *Beppo-SAX*, GRO J1008−57 (Naik et al. 2011), and 1A 1118−61 (Maitra et al. 2012) with *Suzaku*. Dips in the pulse profile can be naturally explained due to the absorption in the accretion stream that is phase locked with the neutron star. The X-ray continuum spectrum of Vela X-1 has been modeled with a power law with an exponential cutoff (White et al. 1983; Tanaka 1986) or with a Negative Positive EXponential model

(Orlandini et al. 1998; Kreykenbohm et al. 1999, 2002). The continuum is further modified by a considerable amount of photoelectric absorption at low energies which varies erratically on short timescales and also with the orbital phase (Haberl & White 1990). A strong iron fluorescence feature at ∼6.4 keV has also been reported (Watanabe et al. 2006).

An absorption like feature at ∼55 keV was first reported by Kendziorra et al. (1992) using data from *HEXE*. This was interpreted as a Cyclotron Resonance Scattering Feature (CRSF). The CRSF arises due to resonant scattering of electrons in Landau levels in the presence of high magnetic fields. The energy of the CRSF is given by $E_c = 11.6 \, \text{keV} \times 1/(1+z) \times (B/10^{12} \, \text{G})$, where E_c is the centroid energy, z is the gravitational redshift, and B is the magnetic field strength of the neutron star. The CRSF therefore gives us an estimate of the magnetic field strength of the neutron star. Pulse-phase-resolved spectroscopy of the CRSF parameters can provide crucial information on the magnetic field geometry and the emission region of the neutron star as we probe it at different viewing angles with spin phase. Makishima & Mihara (1992) and Choi et al. (1996) reported an absorption feature at ∼32 keV from the *Ginga* data. Mihara (1995) performed a detailed analysis of the *Ginga* observations and found that the CRSFs vary in strength over the pulse phase. Kretschmar et al. (1997) also confirmed the existence of two absorption features at ∼23 keV and ∼45 keV using the broadband data from the *HEXE* and TTM, and found similar variations with pulse phase as from the *Ginga* data. Subsequently more detailed pulse-phase-resolved analysis was performed by Kreykenbohm et al. (1999, 2002) using *RXTE* data who confirmed the existence of the two lines at ∼25 and 55 keV and also reported their variation with the pulse phase. Orlandini et al. (1998) and La Barbera et al. (2003) performed phase-resolved analysis of Vela X-1 using *BeppoSAX* data but could only confirm the existence of the absorption line at ∼55 keV.

We present here a pulse-phase-resolved spectral analysis of Vela X-1 using *Suzaku* observation in 2008 June. The same *Suzaku* observation has been analyzed by Doroshenko et al. (2011) who have mainly focused on the three off-states detected for a few pulses during the observation, and have

---

[1] Joint Astronomy Programme, Indian Institute of Science, Bangalore 560012, India.

detected pulsations for the first time in these "off-states". They have also analyzed the energy-dependent pulse profiles and the energy spectrum in both the off and normal states, and have confirmed the presence of the two CRSFs in the normal states. We have however probed the energy dependence of the pulse profiles in much more detail and carried out pulse-phase-resolved spectroscopy in narrow phase bins to explore its complex nature. The variations of the continuum spectral parameters as well as the CRSF fundamental and harmonic with pulse phase reported here are the most detailed results available so far. While performing pulse-phase-resolved analysis, care has also been taken to average over data having similar intensity and spectral hardness, to probe the variation solely due to the changing viewing angle with pulse phase. In Section 2 we describe the observation and data reduction, in Section 3 the pulse profiles including their energy and intensity dependence; in Section 4 spectroscopy, including phase averaged and phase resolved, followed by discussions and conclusions in Section 5.

2. OBSERVATIONS AND DATA REDUCTION

Vela X-1 was observed with *Suzaku* (Mitsuda et al. 2007) on 2008 June 17 and 18 (ObsID: 403045010). The observation (exposure ∼103 ks) was performed at "HXD nominal" pointing position. *Suzaku* has two sets of instruments on board, the X-ray Imaging Spectrometer (XIS; Koyama et al. 2007) covering the 0.2–12 keV range, the Hard X-ray Detector (HXD) having PIN diodes (Takahashi et al. 2007) covering the energy range 10–70 keV, and GSO crystal scintillator detectors covering the 70–600 keV energy band. The XIS consists of four CCD detectors, three of which are front illuminated (FI: XIS0, XIS2, XIS3) and one back illuminated (BI: XIS1). Since the loss of XIS2 in 2006 November, only XIS 0, 1, and 3 are operational. For this observation, the XISs were operated in "Normal" clock mode in the "1/4 window" option which gave a time resolution of 2 s.

HEASOFT 6.11 was used for the reduction and extraction. For the reduction and extraction of the XIS data, the unfiltered XIS events were reprocessed with the CALDB version 20100123 for XIS and 20091007 for HXD. The reprocessed XIS event files were then checked for the possible presence of photon pileup. Pile-up estimation was performed by examining the point-spread function (PSF) of the XISs by checking the count rate per one CCD exposure at the image peak as given by Yamada & Takahashi.[2] Following their procedure, the value obtained was higher than that of the Crab Nebula count rate of 36 count arcmin^{-2} s^{-1} (CCD exposure), and the radius at which this value equals 36 in the PSF is about 15–16 arcsec. Thus the check performed showed a case of moderate photon pile-up, and 15 pixels from the image center were removed to account for this effect. For the extraction of XIS light curves and spectra from the reprocessed XIS data, a circular region of 4′ diameter was selected around the source centroid with the central 15 (∼16″) pixels removed. Background light curves and spectra were extracted by selecting a region of the same size away from the source. The XIS count rate after the pile-up correction was around ∼34 counts s^{-1} with ∼12% of the photons being lost due to the removal of the photons from the central region. Response files and effective area files were generated by using the FTOOLS task "xisresp." For extracting HXD/PIN light curves and spectra, cleaned event

files were used (processing version 2.2.8.20). For HXD/PIN background, simulated "tuned" non-X-ray background event files corresponding to 2008 June were used to estimate the non-X-ray background,[3] and the cosmic X-ray background was simulated as suggested by the instrument team[4] applying appropriate normalizations for both cases. Response files of the respective observations were obtained from the *Suzaku* guest observatory facility.[5]

3. TIMING ANALYSIS

For the timing analysis, we applied barycentric corrections to the event data files using the FTOOLS task "aebarycen." Light curves with a time resolution of 2 s and 1 s were extracted from the XISs (0.2–12 keV) and the HXD/PIN (10–70 keV), respectively. Pulsations were searched for in the data by applying pulse folding and χ^2 maximization technique. The best estimate of the period was found to be 283.24 ± 0.16 s. We also checked for the correction of the pulse arrival times due to the orbital motion of the neutron star which showed that the filtered events corresponded to an orbital phase ∼0.17–0.36. The orbital motion curve however fitted well to a straight line in this phase range. This implies only a linear correction in the pulse arrival times which would not alter our results on pulse-phase-resolved spectroscopy significantly. Thus, orbital correction for the pulse arrival times was not required. The pulse period has been determined for the same data set to a greater precision by Doroshenko et al. (2011). Figure 1 shows the average pulse profile of Vela X-1 created by folding the light curve with the obtained pulse period.

3.1. Light Curves and Hardness Ratio

Figure 2 shows the light curves of Vela X-1 rebinned with the time bin equal to the pulse period as obtained from the XIS and PIN data, respectively. The light curves show that the source is highly variable. Panel 3 of the same figure shows the hardness ratio (ratio of PIN counts to XIS counts) for the entire stretch. Except for the brief initial stretch at the beginning, the hardness ratio remains nearly constant up to the first 90,000 s after which it is more variable with an increasing trend. For this above-mentioned constant hardness ratio stretch, arrows in panel 1 also show the "off-states" in the XIS light curve as presented in Doroshenko et al. (2011). Since the main aim of this work is to perform pulse-phase-resolved spectroscopy to probe the spectral parameters with changing viewing angle, we took only this stretch of constant hardness ratio excluding the "off-states" for further analysis. This would ensure that our results would be free from any systematic effects of phase average spectral variability.

3.2. Intensity Dependence of the Pulse Profiles

As already mentioned earlier, since the main aim of this work is to probe the pulse phase dependence of the spectral parameters, we also checked for the intensity dependence of the pulse profiles to avoid averaging over data having different luminosity dependence. Intensity-dependent pulse profiles were created using both XIS (0.3–12 keV) and PIN (10–70 keV) for the above-mentioned stretch of the data having similar hardness ratio and excluding the "off-states." Pulse profiles were created
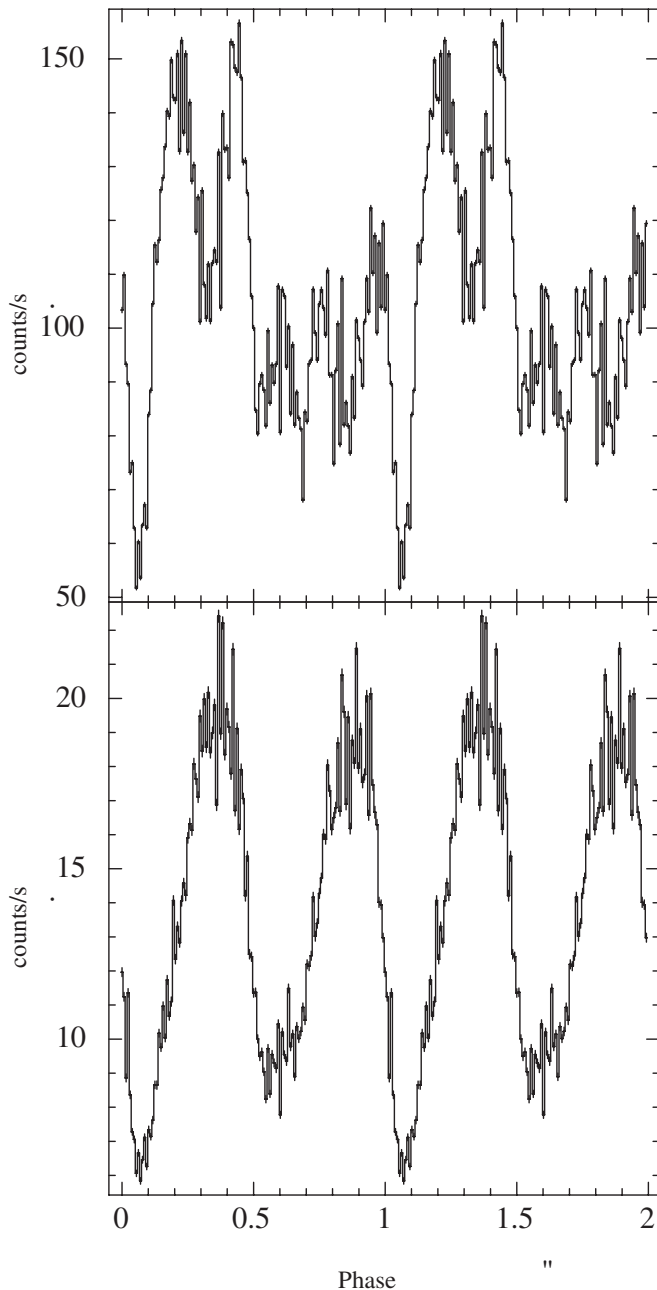

Figure 1. Average pulse profile of Vela X-1 folded with the best obtained period. The top panel shows the pulse profile (0.3–12 keV) using XIS data and the bottom panel shows the pulse profile (10–70 keV) using PIN data.

3.3. Energy Dependence of the Pulse Profiles

Energy-resolved pulse profiles were created by folding the light curves in different energy bands with the obtained pulse period. In light of the issues discussed in the above sections, pulse profiles were created for the constant hardness ratio stretch excluding the "off-states" and in the intensity band of $\leqslant 50\,\mathrm{s}^{-1}$. This is different from that presented by Doroshenko et al. (2011) who have compared the energy-resolved pulse profiles between the on and "off-states." Our main goal is to avoid the systematic effects which might affect our results of pulse-phase-resolved spectroscopy described later in Section 4.2. The energy dependence of the pulse profiles is shown in Figure 4. The pulse profiles from 0.3 to 12 keV are created using all the three XISs (0, 1, and 3). Higher energy profiles are created from the PIN data. The figure shows that the pulse profiles have complex energy-dependent structures, with up to five peaks in the XIS energy band which merge to two asymmetric peaks in the PIN energy band. With a careful examination of the pulse profiles, the following characteristics can be observed (refer to Figure 4 for the exact location of the low-energy peaks).

1. The first two peaks in the low-energy profiles at phases ∼0.2 and 0.5 (henceforth termed peaks a and b) merge to become a single asymmetric peak (phase ∼0.3) at $\geqslant 12$ keV. The next three peaks of the low-energy profiles at phases ∼0.6, 0.8, and 1 (henceforth termed peaks c–e) merge to become the second high-energy peak (phase ∼0.9) after 12 keV.
2. The dip at phase ∼0.3 between the peaks a and b decreases with energy and disappears at ∼12 keV.
3. The dip at phase ∼0.7 between the peaks c and d however increases with energy up to 5 keV after which it shows a decreasing trend and disappears at ∼14 keV.
4. The dip at phase ∼0.9 between the peaks d and e also decreases with energy and disappears at ∼7 keV.
5. There is also an indication of a dip-like structure at the lowest energies (⩽5 keV) between phases 0.5–0.6.

4. SPECTROSCOPY

4.1. Pulse-phase-averaged Spectroscopy

We performed pulse-phase-averaged spectral analysis of Vela X-1 using spectra from the front-illuminated CCDs spectrum (XIS 0 and 3), back-illuminated CCD spectrum (XIS 1), and the PIN spectrum. As discussed earlier we extracted spectra only for the above mentioned stretch of the data having similar hardness ratio, excluded the "off-states," and further applied intensity filtering to choose the time within it having count rates $\leqslant 50$ counts s^{-1}. Spectral fitting was performed using *XSPEC* v12.7.0. The energy ranges chosen for the fits were 0.8–10 keV for the XISs and 12–70 keV for the PIN spectrum. Due to an artificial structure in the XIS spectra around the Si edge and Au edge, the energy range of 1.75–2.23 keV was neglected. After appropriate background subtraction we fitted the spectra simultaneously with all parameters fixed, except the relative instrument normalizations which were kept free. The XIS spectra were rebinned by a factor of six from 0.8 to 6 keV and 7 to 10 keV, and by a factor of two between 6 and 7 keV. The PIN spectra were rebinned by a factor of two up to 22 keV, by four up to 45 keV, and six up to 70 keV.

The continuum was fitted with both a phenomenological high-energy cutoff "highecut" model and a more physical

in three intensity windows having characteristic XIS count rates ⩽20 counts s^{-1}, 20–50 counts s^{-1}, and ⩾50 counts s^{-1} by applying intensity filtering. Figure 3 shows the intensity-dependent pulse profiles in the XIS and PIN energy bands, respectively. The XIS and the PIN profiles also show similar characteristics in all the intensity bands except for a slightly larger pulse fraction in XIS at low count rate (⩽20) and in PIN at medium count rate (20–50). The XIS pulse profile created with counts greater than 50 however differs considerably, with the dips and peaks in some phases not coinciding; as can be seen from the figure, the dip in the highest intensity profile at phase ∼0.6 coincides with a peak in the other intensity band profiles. To avoid this intensity dependence, we averaged over data only in the intensity band of ⩽50 counts s^{-1} to perform spectral analysis.
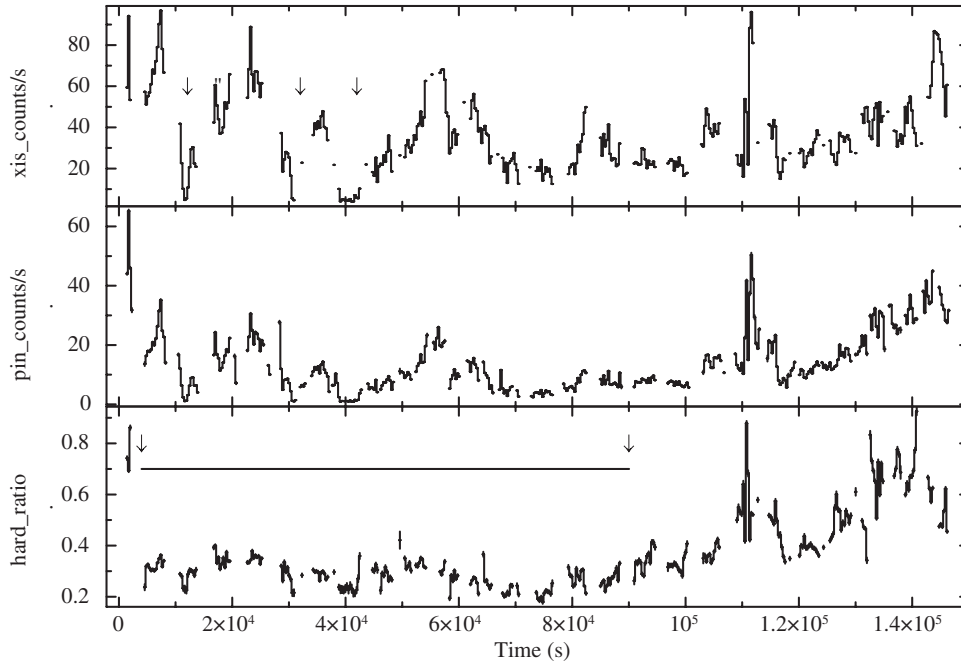
Figure 2. The top panel shows the light curve of Vela X-1 obtained with *Suzaku* for one of the XIS in the energy band of 0.3–12 keV. The middle panel shows the same obtained in the PIN energy band (10–70 keV). The time binning is equal to the pulse period. The bottom panel shows the hardness ratio. The arrows and the dash indicate the time range of the data which were selected on the basis of constant hardness ratio for further analysis.

Comptonization model "CompTT" assuming a spherical geometry for the Comptonizing region (Titarchuk 1994). In both the cases along with the Galactic line-of-sight absorption, a partial covering absorption model "pcfabs" was applied to take into account the intrinsic absorption local to the neutron star. A Gaussian line was also used to model the narrow Fe Kα feature found at 6.4 keV. In addition, two absorption features were found at 25 and 50 keV, which are the CRSF fundamental and harmonic as found previously for this source. These were modeled with Lorentzian profiles. Figure 5 shows the best-fitting spectra along with the residuals. Since the energy spectrum has a strong pulse phase dependence, we do not expect the pulse-phase-averaged spectrum to fit well to a simple continuum model. The best-fitting parameters for the high-energy cutoff "highecut" model and the "CompTT" model are given in Table 1. The best fit had a reduced χ^2 of 2.03 for 831 dof for the "highecut" model and 1.92 for 832 dof for the "CompTT" model. The value of the additional absorption component (N_{H2}) and the covering fraction (Cv_{frac}) are higher for the "CompTT" model. The fundamental CRSF has similar parameters for both the models except for a slightly wider line in the case of the "CompTT" model. The harmonic is however much deeper and wider in the case of the "CompTT" model. The continuum model used by Doroshenko et al. (2011) is slightly different from ours since they used a combination of power law and CompTT model while we have used a partial covering CompTT model. As a result, the Galactic line-of-sight absorption (N_{H1}) value obtained in our analysis is lower, and the Comptonization parameters are also different. The cyclotron parameters however match well and are consistent with each other within error bars. Keeping in mind that Ecycl from the Lorentzian description does not define the minimum of the line profile (Nakajima et al. 2010), from the values of $E1_{cycl}$ and $E2_{cycl}$ we obtained with the Lorentzian (cyclabs) model, the corresponding minima of the line profile are calculated to be at 26.8 keV and 56.3 keV which are consistent with the values obtained by Doroshenko et al. (2011) within error bars. The depth and width of the cyclotron lines are also consistent.

Table 1
Best-fitting Spectral Parameters of Vela X-1 with a Partial Covering
High-energy Cutoff Model

Parameter	Highecut Model Values	CompTT Model Values
N_{H1} (10^{22} atoms cm^{-2})	1.38 ± 0.01	$1.05^{+0.017}_{-0.016}$
N_{H2} (10^{22} atoms cm^{-2})	$4.00^{+0.27}_{-0.26}$	$6.30^{+0.30}_{-0.29}$
Cv_{frac}	0.385 ± 0.01	0.451 ± 0.008
PowIndex	1.19 ± 0.005	$\cdots$
E-folding energy (keV)	$16.07^{+1.66}_{-1.47}$	$\cdots$
E-cut energy (keV)	$24.56^{+0.80}_{-0.78}$	$\cdots$
powerlaw$_{norm}$[a]	0.190 ± 0.001	$\cdots$
CompTT$_{T0}$ (keV)	$\cdots$	0.49 ± 0.007
CompTT kT (keV)	$\cdots$	10.59 ± 0.14
CompTT τ	$\cdots$	10.95 ± 0.099
CompTT$_{norm}$[a]	$\cdots$	0.062 ± 0.0004
$E1_{cycl}$ (keV)	$24.10^{+1.05}_{-0.99}$	$24.42^{+1.68}_{-1.57}$
$D1_{cycl}$	0.26 ± 0.04	0.28 ± 0.05
$W1_{cycl}$ (keV)	$4.37^{+1.86}_{-1.39}$	$7.70^{+2.97}_{-2.27}$
$E2_{cycl}$ (keV)	$50.53^{+3.36}_{-2.74}$	$48.70^{+1.29}_{-1.23}$
$D2_{cycl}$	$0.94^{+0.33}_{-0.28}$	$1.82^{+0.18}_{-0.17}$
$W2_{cycl}$ (keV)	$10.00^{+4.28}_{-3.28}$	$19.27^{+3.80}_{-2.92}$
Iron line energy (keV)	6.41 ± 0.01	6.41 ± 0.01
Iron line eqwidth (eV)	56.8 ± 2.3	56.7 ± 2.2
Flux (XIS)[b] (0.3–10 keV)	1.53 ± 0.01	1.53 ± 0.01
Flux (PIN)[b] (10–70 keV)	4.12 ± 0.01	4.11 ± 0.01
Reduced χ^2/dof	2.03/831	1.92/832

Notes. Errors quoted are for 99% confidence range.
[a] photons keV^{-1} cm^{-2} s^{-1} at 1 keV.
[b] Flux is in units of 10^{-9} erg cm^{-2} s^{-1} and is in 99% confidence range.

Confidence contours were plotted to check the interdependence between some of the parameters for both the models. Figure 6 shows the χ^2 confidence contours between several pairs of model parameters for the phase-averaged spectra. Among the continuum parameters when both were allowed to vary, the partial covering parameters N_{H2} and Cv_{frac} could be constrained
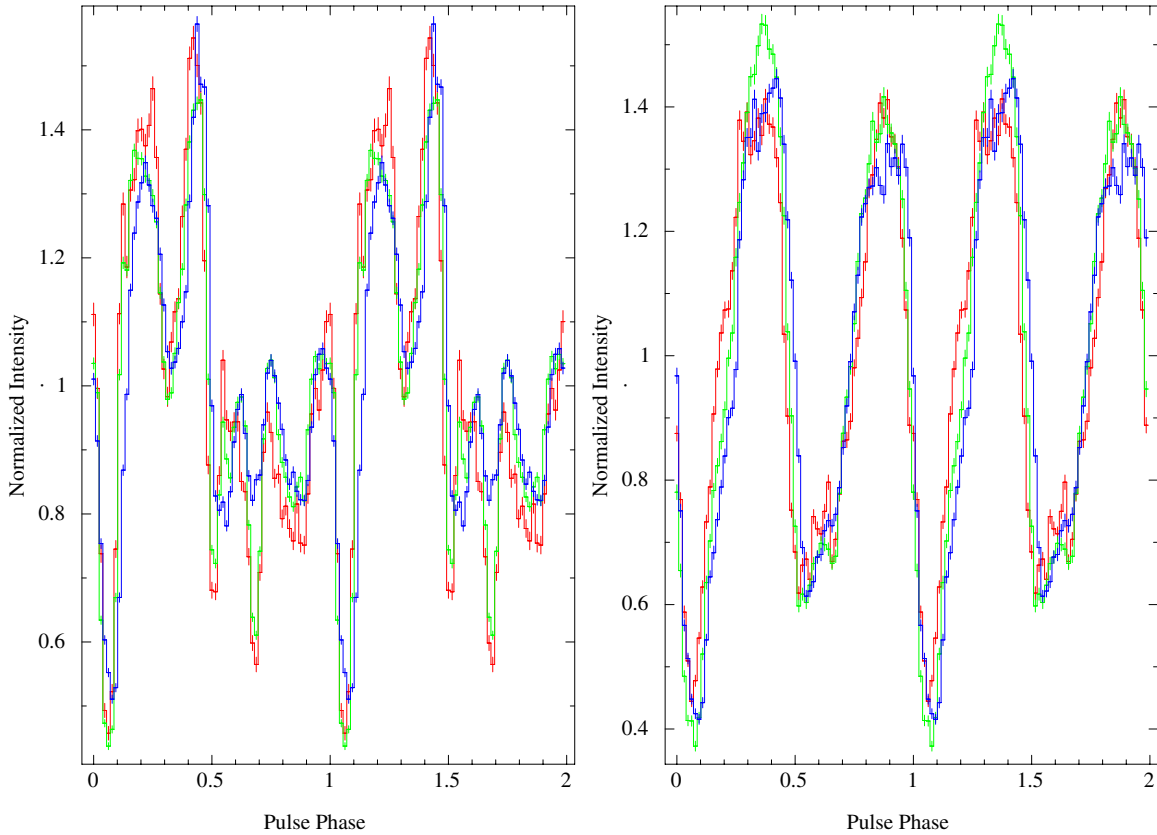
Figure 3. Intensity-dependent pulse profiles of Vela X-1. The left panel shows the pulse profiles (0.3–12 keV) using XIS data and the right panel shows the pulse profile (10–70 keV) using PIN data. The pulse profile in red shows the profile with XIS count rate $\leqslant$20 counts s^{-1}, the one in green with 20–50 counts s^{-1}, and the one in blue $\geqslant$50 counts s^{-1}.

well within 14% and 8% of the respective parameter values for the "highecut" model. There were however limitations in this model such as that the break energy "E-cut" and the fundamental CRSF $E1_{\rm cycl}$ were found to be correlated and could not be well constrained independently. The contour between $E1_{\rm cycl}$ and the power-law photon index (Γ) showed that although Γ could be constrained very well, $E1_{\rm cycl}$ could not be. The fundamental being very shallow, and possibly because of the correlation with the break energy and inability to constrain against Γ in the "highecut" model, the energy and depth of the fundamental could not be constrained completely independent of these parameters. However, similar trends of the variation of the fundamental line energy obtained with pulse phase for both the models give us added confidence in our results. $N_{\rm H2}$ and $C v_{\rm fract}$ for the "CompTT" model also could be constrained well (11% and 6% of their values). The optical depth and electron temperature "τ" and "kT" showed some correlation but could be constrained between 18% and 4% of their values. The interdependence between the parameters discussed above was also evident from the results of the pulse-phase-resolved spectroscopy of the parameters discussed later. For the cyclotron line parameters, both the CRSFs could be constrained well in the case of the "CompTT" model and showed no dependence either among themselves or with the continuum parameters like "τ" and "kT." In the case of the "highecut" model although parameters of the CRSF harmonic could be constrained well, the $E1_{\rm cycl}$ and $D1_{\rm cycl}$ contour maps showed dependency and difficulty in constraining both the parameters simultaneously. However, the similar trend of variation of the parameters obtained with both the spectral models as discussed above gives us confidence in our obtained

results. Because of some of the limitations discussed here, the errors quoted and plotted henceforth are assuming variation of only one parameter, with the other parameters allowed to vary independently to find the minimum χ^2.

4.2. Pulse-phase-resolved Spectroscopy

Strong energy dependence of the pulse profiles, as shown in Figure 4, implies dependence of the energy spectrum on the pulse phase. The narrow energy-dependent dips in the pulse profiles can also be explained by a partial covering absorption model in which the absorber is phase locked with the neutron star. To investigate this we performed pulse-phase-resolved spectroscopy, applying phase filtering in the FTOOLS task XSELECT. For the phase-resolved analysis, we used the same background spectra and response matrices as were used for the phase-averaged spectrum for both the XISs and the PIN data. We also fitted the spectra in the same energy range and rebinned them by the same factor as in phase-averaged case. The value of the Galactic absorption ($N_{\rm H1}$) and the Fe line width were frozen to the phase-averaged values for the two respective models.

4.2.1. Phase-resolved Spectroscopy of the Cyclotron Parameters

To investigate the pulse-phase-resolved spectroscopy of the two CRSFs, we generated phase-resolved spectra with the phases centered as in the case of 25 independent bins but at thrice their widths. This resulted in 25 overlapping bins out of which only 8 were independent. Due to limited statistics we were unable to constrain all the parameters, and froze the width of the
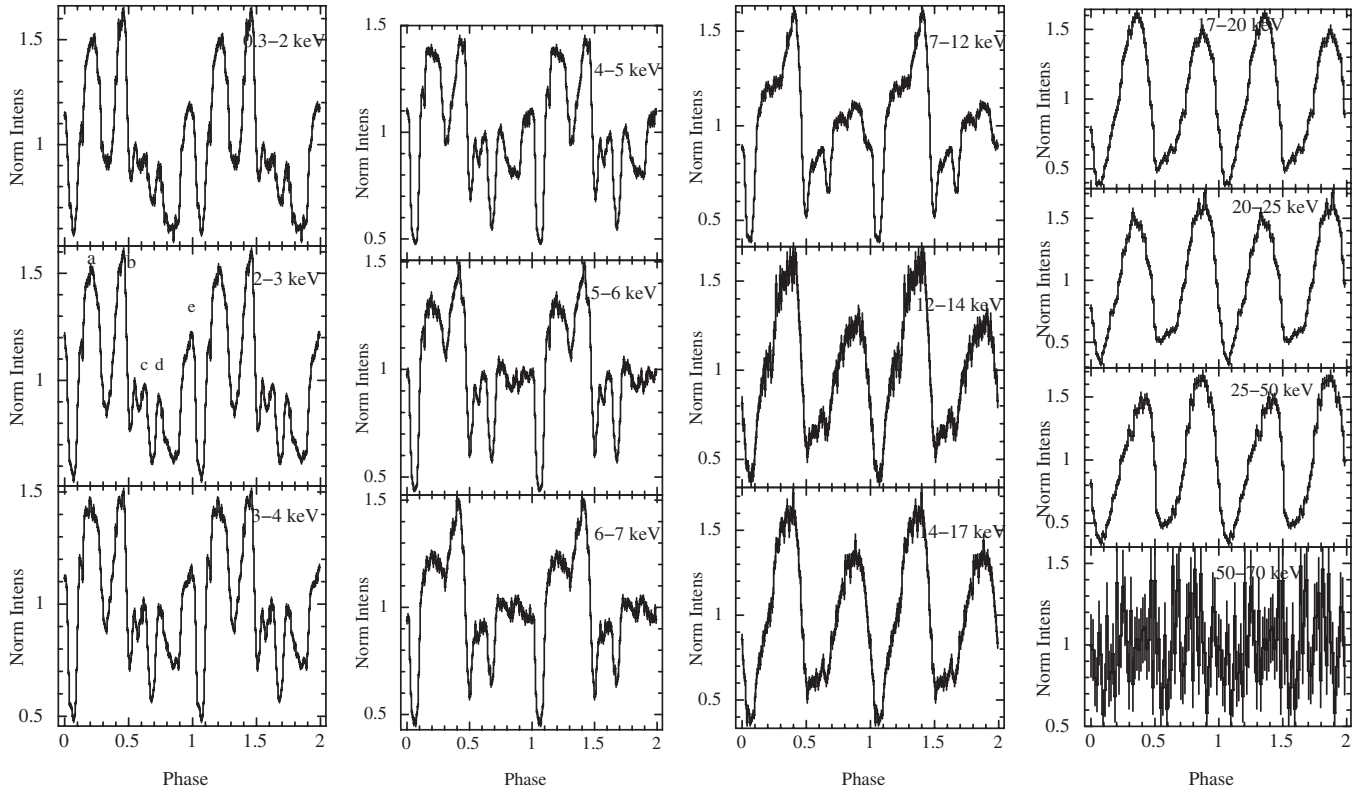
Figure 4. Energy-dependent pulse profiles of Vela X-1 using XIS and PIN data. The energy ranges for the pulse profiles are specified inside the panels.
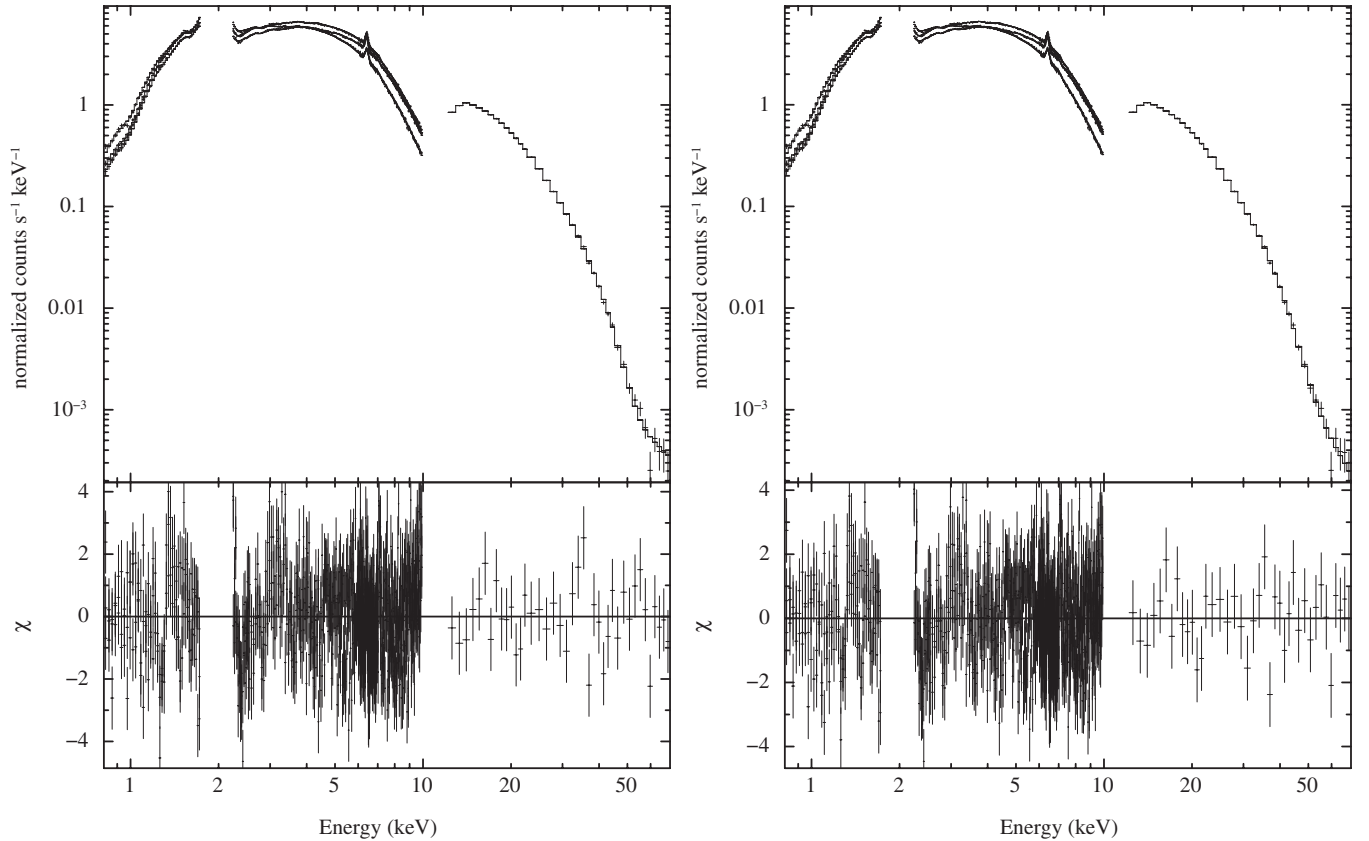

Figure 5. Pulse-phase-averaged spectrum of Vela X-1 using high-energy cutoff model (left panel) and "CompTT" model (right panel). The upper panel shows the best-fit spectra. The residuals are given in the bottom panels.
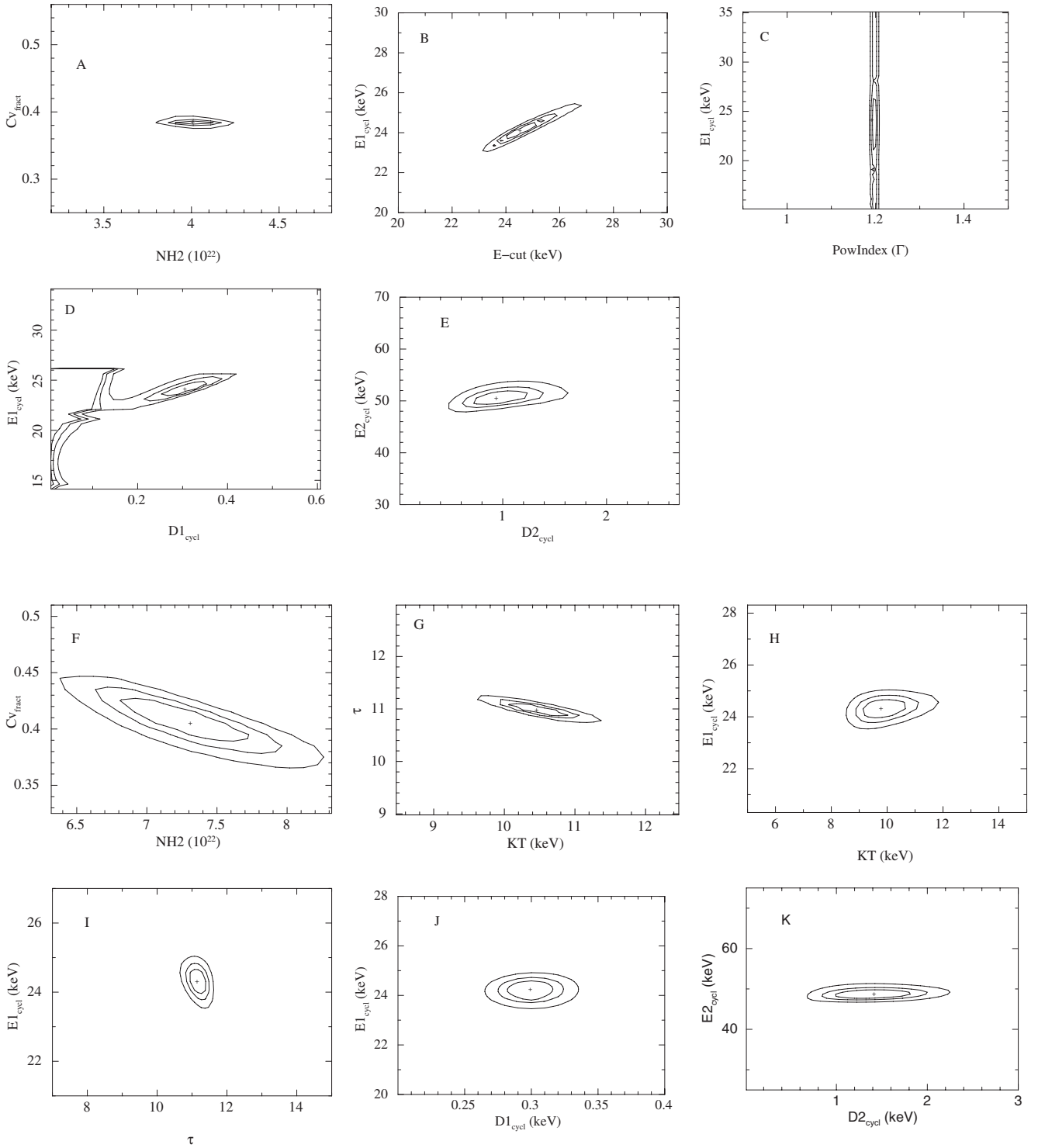
Figure 6. χ^2 confidence contours between several pairs of continuum and line parameters for the two models, obtained from the phase-averaged spectra. The innermost to outermost contours represent respectively 68%, 90%, and 99% confidence levels. The upper five panels show the contour plots for the "highecut" model and the lower six panels for the "CompTT" model. The plots show the confidence contours between (A) N_{H2} and Cv_{fract}, (B) E-cut energy and $E1_{cycl}$, (C) PowIndex and $E1_{cycl}$, (D) $E1_{cycl}$ and $D1_{cycl}$, and (E) $E2_{cycl}$ and $D2_{cycl}$, for the "highecut" model, and (F) N_{H2} and Cv_{fract}, (G) τ and kT, (H) $E1_{cycl}$ and kT, (I) $E1_{cycl}$ and τ, (J) $E1_{cycl}$ and $D1_{cycl}$, and (K) $E2_{cycl}$ and $D2_{cycl}$, for the "CompTT" model.

CRSF harmonic to the phase-averaged value of the respective models and varied the rest of the parameters with pulse phase. For phases close to or at the off pulse regions, the CRSFs are weak and sometimes cannot be detected in the spectra for either or both of the continuum models. Confidence contours were created for the pairs of parameters as shown in panels B, C, D, E, H, I, J, K in Figure 6 for some of the phase-resolved spectra. The fundamental $E1_{cycl}$, when paired with the parameters $D1_{cycl}$, E-cut, or Γ, could not be constrained simultaneously as was the case with the phase-averaged spectrum. For all the other
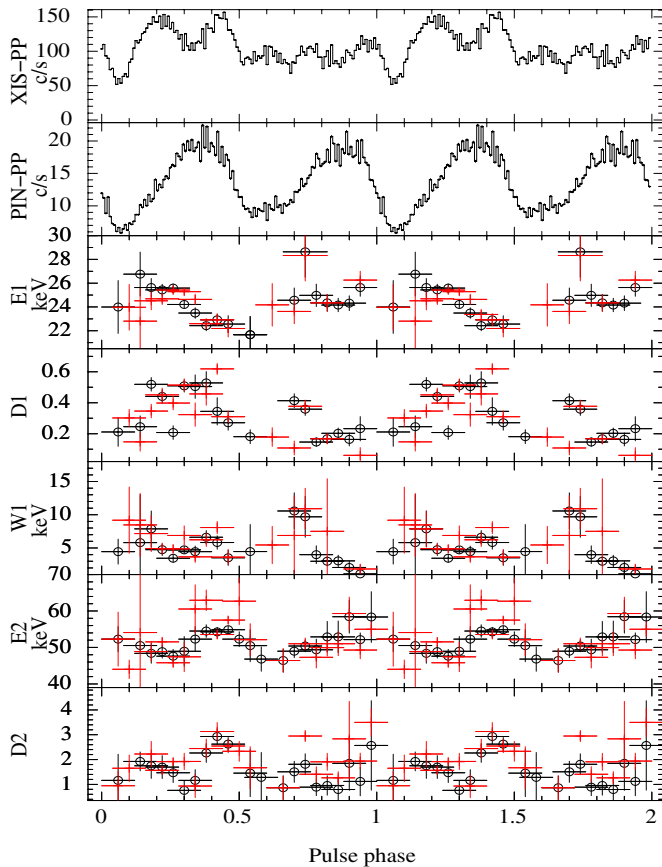
Figure 7. Variation of the cyclotron line parameters as is obtained with the two models. The black points with "circle" denotes the parameters as obtained with the highecut model The red points denote the points as obtained with the CompTT model. Only 8 of the 25 bins are independent. Although the parameters for the two models match reasonably well, the fundamental line energy for the highecut model cannot be constrained well and depends on the continuum parameters, especially the cutoff energy as shown in the contour plots in Figure 6.

pairs, the parameters could be constrained fairly well with the errors being ~1.5 times the corresponding errors with the phase-averaged spectrum. Refer to Section 4.1.

Figure 7 shows the variation of the cyclotron parameters for both the models as a function of pulse phase. Despite statistical limitations in the data to constrain the CRSF fundamental energy and depth independent of the cutoff energy in the "highecut" model, the variation of the CRSF parameters has a very similar pattern for both the "highecut" and the "CompTT" model. This gives us a reasonable amount of confidence in the obtained results. The results also follow the trend as obtained previously by Kreykenbohm et al. (2002) using *RXTE* but they did not have enough sensitivity to probe these features in detail. The following features can be seen from Figure 7. The variation is compared with respect to the high-energy PIN pulse profile shown in panel two of the same figure and the peaks and dips refer to the peaks and dips in the same.

1. The energy of the fundamental ($E1_{cycl}$) varies by a large amount with pulse phase, with the values varying between 22 keV in the off pulse region and 28 keV in the ascending phase of the second pulse. It has a decreasing trend with phase for the first pulse with nearly constant values for the second pulse, except for the ascent of the second pulse at phase ~0.7 where $E1$ peaks in value.

2. The depth of the fundamental ($D1_{cycl}$) varies by almost a factor of three with the pulse phase, with the deepest lines near the pulse peaks and shallowest in the off pulse regions. Its value peaks near the ascending edges of the first pulse (phase ~0.2–0.4) and the ascending edge of the second pulse (phase ~0.7). The lines are in general deeper for the first pulse.

3. The width ($W1_{cycl}$) of the fundamental varies by almost a factor of two. The width is maximum at the rising edges of the two pulse peaks at phases ~0.1 and 0.7.

4. The energy of the second harmonic ($E2_{cycl}$) varies between values of 48–62 keV. The values are maximum at the descending phase of both the pulses.

5. The depth of the second harmonic ($D2_{cycl}$) varies by a factor of two with the deepest harmonics found at the same phases as the phases having maximum $E2_{cycl}$.

6. The ratio of the two line energies $E1_{cycl}/E2_{cycl}$ has significant pulse phase dependence (Figure 8) with an average value of ~2.1, maximum of ~2.6 near the pulse peaks at phase ~0.4 and ~0.9, and minimum of ~1.7 near the off pulse regions at phase ~0.8.

4.2.2. Phase-resolved Spectroscopy of the Continuum Parameters

To investigate the pulse-phase-resolved spectroscopy of the continuum parameters we generated the phase-resolved spectra with 25 independent phase bins. We froze the cyclotron parameters of the corresponding phase bins to the best-fit values obtained for the investigation of the cyclotron line parameters using 25 overlapping phase bins as described in Section 4.2.1. Figure 9 shows the best-fit phase-resolved continuum parameters for both the models as a function of the pulse phase. Confidence contours were created for the pairs of parameters as shown in panels A, F, and G in Figure 6 for some of the phase-resolved spectra. For all the pairs, the parameters could be constrained well with the errors being ~1.3 times the corresponding errors with the phase-averaged spectrum. Refer to Section 4.1. The results obtained as seen from the figure from both the models are as follows.

1. At the dips between peaks a and b (phase ~0.3) and peaks d and e (phase ~0.9) of the low-energy XIS profile, there is a sudden increase in the value of the local absorption component (N_{H2}). The dip being larger at phase 0.3, the corresponding value of N_{H2} is also larger.

2. At the main dip of the XIS profile between phase 0.5–0.6, there is also an indication of an increase of N_{H2} with a high covering fraction (Cv_{fract}).

3. The dip between c and d (phase ~0.7) of the XIS profile has somewhat different characteristics and extends up to 20 keV. The "highecut" model shows a very high value of N_{H2} and a very small Cv_{fract} at this phase. The "CompTT" model however does not show any significant change in the values of N_{H2} or Cv_{fract}, but a very high optical depth (τ).

4. The value of Cv_{fract} shows a somewhat different pattern of variation for the two models. For the "highecut" model, the phases where N_{H2} is high usually have a small Cv_{fract}, but for the "CompTT" model there is an indication of correlation between the two parameters.

5. In general, the optical depth (τ) increases and the low-energy seed temperature CompTT$_{T0}$ falls at the dips of the XIS pulse profile.

6. The power-law photon index (Γ) shows a strong dependence on the pulse profile. It is hardest at high-energy PIN pulse
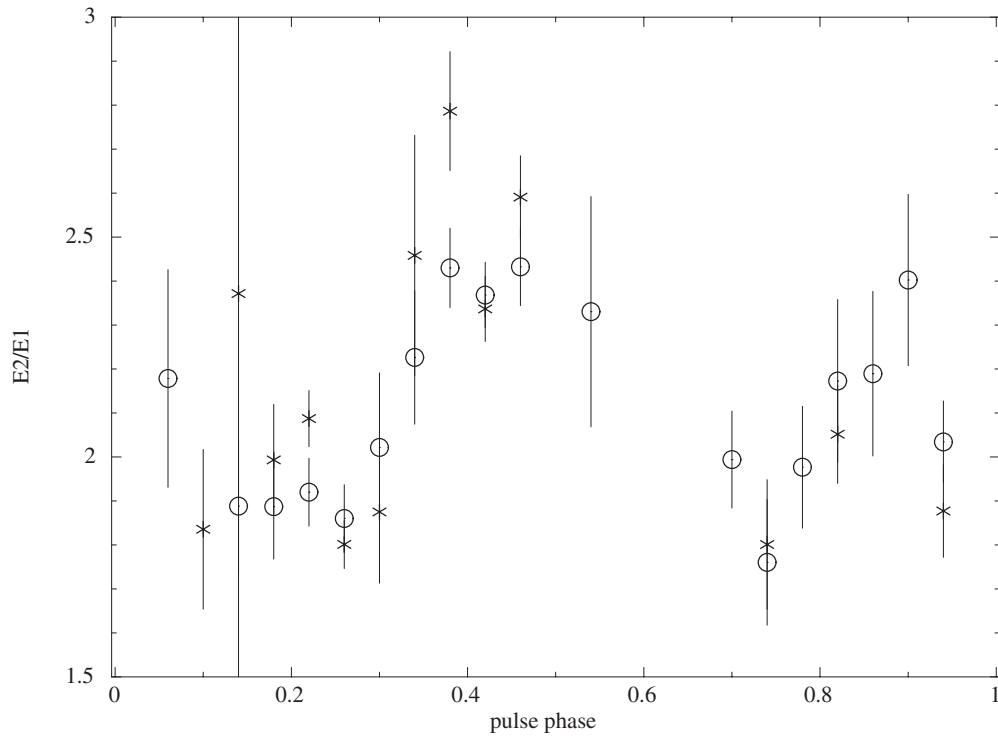
Figure 8. Variation of the ratio of the two cyclotron lines E2/E1 as is obtained by fitting the two models. The variation of the parameter as obtained from the high-energy cutoff model is denoted by the symbol "circle." Variation of the parameter as obtained from the CompTT model is denoted by the symbol "star."

profile peaks and softest at the off pulse phases. Similar spectral hardening at the pulse peaks was found for this source previously by Kreykenbohm et al. (1999).

7. The folding energy (E_{fold}) varies with the pulse phase with the values peaking at the ascending and descending phases of the PIN pulse profile, and their minimum at the pulse peaks. The cutoff energy also varies with the pulse phase.

8. The electron temperature (kT) is highest at the ascending and descending phases of the PIN pulse profile at phases $\sim$0.1, 0.5, 0.7, and 1. It is lower in the off pulse regions.

9. The optical depth (τ) and kT however show strong anti-correlation with each other throughout the pulse phase. This may imply that the statistics of the data are not good enough to determine the variation of these two parameters independently as was already indicated in the confidence contour maps.

10. Both the power-law normalizations (powerlaw$_{norm}$) and the CompTT normalizations (CompTT$_{norm}$) show a variability pattern with the values peaking at the peaks of the XIS pulse profile.

5. DISCUSSIONS AND CONCLUSIONS

In the present work, we have performed a detailed pulse-phase-resolved analysis of a long *Suzaku* observation of Vela X-1. Data from the same *Suzaku* observation have been analyzed by Doroshenko et al. (2011). They have probed the energy dependence of the pulse profile in four energy bands and have confirmed the presence of the two CRSFs in the energy spectrum. We have however investigated the complex energy dependence of the pulse profiles and probed the narrow dips of the same in much more detail by performing pulse-phase-resolved spectroscopy. Pulse-phase-resolved spectral analyses have been performed previously by Kreykenbohm et al. (1999, 2002) using *RXTE* data. Apart from the variations in the

continuum spectra with the pulse phase they also confirmed the existence of the two lines at $\sim$25 and 55 keV and reported their variation with the phase. In the present work, we have used a long observation of Vela X-1 with *Suzaku*, and the high sensitivity of *Suzaku* over a broad energy band allows us to carry out the same with much finer phase bins. Orlandini et al. (1998) and La Barbera et al. (2003) performed phase-resolved analysis of Vela X-1 using *BeppoSAX* data but could only confirm the existence of the absorption line at $\sim$55 keV. The results in all these previous works are more or less in agreement with us. But we have been able to bring out these variations in more detail especially for the two CRSFs for which this is the most detailed result obtained so far.

5.1. Energy-resolved Pulse Profiles

Vela X-1 is a highly variable source and shows strong pulse to pulse variations. The low- and high-energy profiles have a very complex structure of up to five peaks at lower energies which eventually merges to become a double-peaked profile at higher energies. The strong energy dependence of the pulse profiles has been probed previously by Doroshenko et al. (2011) using data from the same *Suzaku* observation in four energy bands which show the structure of the complex pulse profiles. Their main emphasis was on comparing the pulse profiles between the on and "off-states." We have however investigated the complex energy dependence of the pulse profiles and probed the narrow dips of the same in much more detail. The presence of double-peaked pulses at high energies has been found previously in some sources, for example in XTE J1946+274 (Paul et al. 2001), 4U 1538−52 (Bildsten et al. 1997), GX 301−2 (Koh et al. 1997) etc. They can either be interpreted due to a fan beam pattern of the emission geometry or that due to the contribution from both the magnetic poles. The low-energy complex pulse profiles are however more difficult to interpret since they are affected
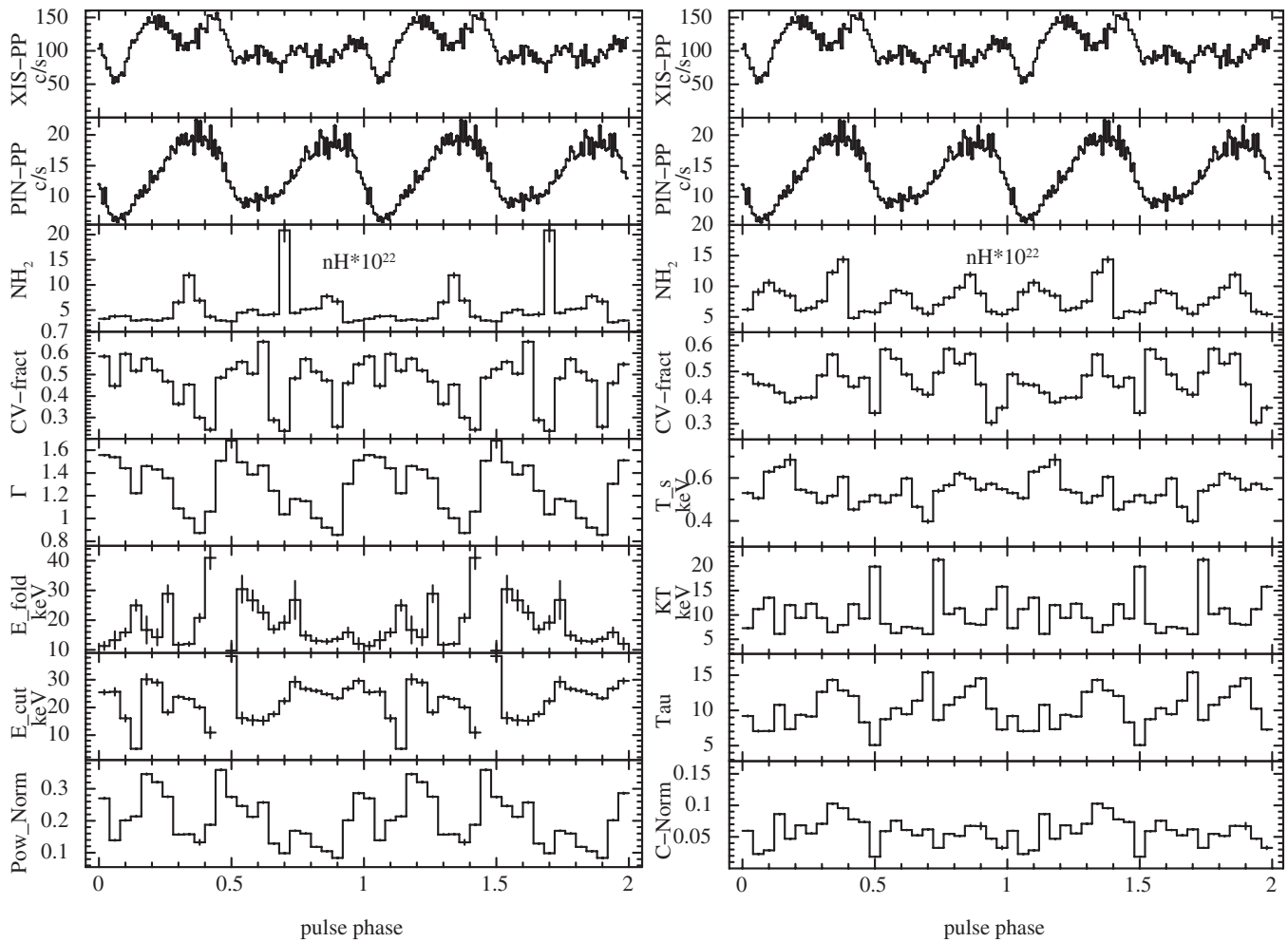
Figure 9. Variation of the spectral parameters with phase along with the pulse profile (0.3–12 keV for XIS and 10–70 keV for PIN). The left panel shows the variation using the model "highecut" and the right panel shows the same using the model "CompTT." For the "highecut" model, the real uncertainty in the value of the cutoff energy is bigger than shown in the plot considering its dependence on the fundamental line energy as seen in the contour plots (Figure 6).

due to scattering and absorption in the local environment of the neutron star. The dips in the low-energy profiles can be explained due to an additional absorption component in our line of sight, probably by the passage of a phase locked accretion stream or the accretion column itself. This aspect is discussed in more detail below.

5.2. Phase-resolved Spectroscopy of the Continuum Spectrum

We have performed pulse-phase-resolved spectroscopy to probe the complex energy dependence of the pulse profiles. The dips in the pulse profiles at phases ∼0.3, 0.5–0.6, 0.7, and 0.9 can be explained due to an increase in the additional absorption column density N_{H2} with a corresponding change in the covering fraction at that phase. The changes in the value of N_{H2} and covering fraction with pulse phase can act as a tracer for the properties of the plasma in the accretion stream, which may be a clumpy structure having different values of opacities and optical depths. The fitted parameters of the "highecut" model show an abrupt increase in the value of N_{H2} at the dips at phases ∼0.3 and 0.9. The dip at phase ∼0.3 extends up to somewhat higher energies, the value of N_{H2} of the former being higher than that at phase ∼0.9. Both of the dips have similar strength in agreement with similar values of covering fraction in both the cases. The main dip at phase 0.5–0.6 may be in-

dicated by a slight increase in N_{H2} with a high value of the covering fraction. The dip at phase ∼0.7 is different from the others since it increases in strength up to 5 keV and then decreases and disappears after 20 keV, being relatively shallower than the other dips in the pulse profile. This dip is in agreement with a large increase in N_{H2} and a very small covering fraction, with the value of N_{H2} peaking at this particular phase. This would indicate the presence of a very dense clump of matter (a narrow and dense stream), with the high value of N_{H2} responsible for the dip extending up to higher energies. In general the covering fraction decreases at the dips in the profile where N_{H2} is larger, which may indicate a clumpy structure of the accretion stream. The "highecut" model is thus able to explain the energy dependence of the pulse profiles very well. The parameters obtained by fitting the spectra with the "CompTT" model, on the other hand, do not show a similar pattern of variation of the partial covering model especially for the case of the covering fraction parameter. The dip at phase ∼0.7 also does not show any significant increase in N_{H2}, although the optical depth (τ) parameter of the "CompTT" model increases at all phases corresponding to the dips. We would however like to point out that the "CompTT" model may not be a good description of the low-energy part of the pulsar spectra keeping in mind that the N_{H2} and the covering fraction were found to have some dependence (mentioned earlier in Section 4.2.2). In addition, it is a highly
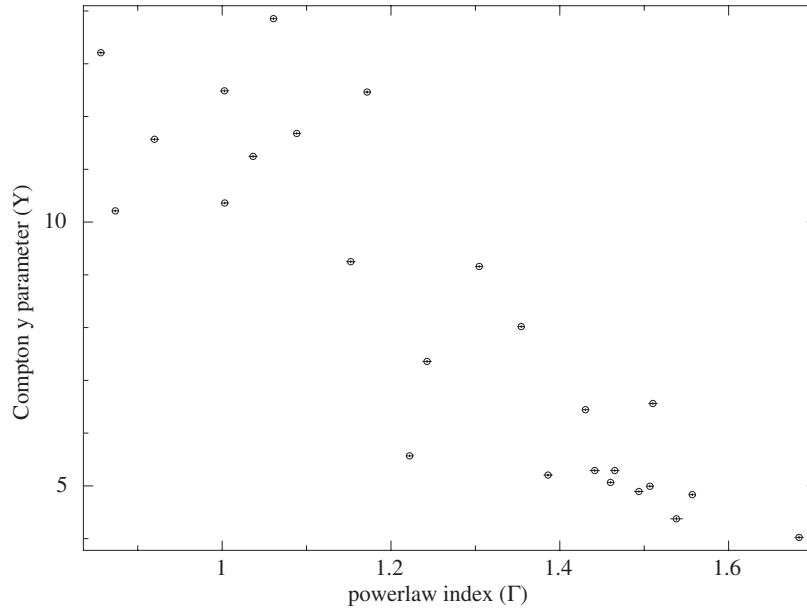
Figure 10. Plot showing the interdependence between the power-law index (Γ) and the Compton Y parameter. The error bars are plotted as seen within the symbols.

simplified model with a spherical shape of the Comptonizing cloud whereas the emission region in accreting pulsars is likely to have a slab or cylindrical geometry. The "highecut" model, in spite of being a phenomenological model and having a divergent property at low energies when paired with a power law, is able to explain the complex energy dependence of the pulse profile better. Another interesting result found is the spectral hardening at the high-energy pulse peaks. The power-law index (Γ) reaches its minima at these phases, more so for the phase corresponding to the second peak (phase ∼0.9). Similar regions of pulse hardening have been observed previously in other sources like Her X-1 (Pravdo et al. 1977, 1978), 4U 0115+63 (Johnston et al. 1978; Rose et al. 1979) and GX 1+4 (Doty et al. 1981), and 1A 1118−61 (Maitra et al. 2012). Assuming the spectral formation by the Comptonization of photons by the thermal electrons, the Compton Y parameter can be used as a measure for the degree of Comptonization. It is given by $y = (4kT_e/m_ec^2)\max(\tau, \tau^2)$, where T_e is the electron temperature and τ is the optical depth. (Rybicki & Lightman 1986). The higher is the degree of Comptonization the larger is the "y" parameter, and hence harder is the spectrum. "y" can be easily found since kT_e and τ are the parameters of the "CompTT" model. Calculating it shows that the "y" values also peak at more or less the same phase as the hardest Γ, i.e., at the pulse peaks with the phase corresponding to the second peak having a higher value of "y." $y \gg 1$ at all the phases, which is indicative of saturated Comptonization being prevalent in the spectrum. We also checked for the correspondence between "Γ" and "y" at all other phases. The parameters seem to be correlated with each other with the Spearman rank correlation coefficient equal to −0.89. Figure 10 shows the interdependence between the two parameters. We would like to caution however that the "CompTT" model assumes spherical geometry for the plasma region, which is a crude approximation for the accretion column which has a cylindrical or slab geometry in most cases. Hence, this may give rise to some systematic errors in the results.

5.3. Phase-resolved Spectroscopy of the Cyclotron Parameters

We also performed pulse-phase-resolved spectral analysis of the two CRSF features. Pulse-phase-resolved spec-

troscopy of the cyclotron parameters has been performed for some sources previously, for example in Her X-1 (Soong et al. 1990; Enoto et al. 2008; Klochkov et al. 2008), 4U 1538−52 (Robba et al. 2001), 4U0115+63 (Heindl et al. 2000), Vela X-1 (Kreykenbohm et al. 1999, 2002; La Barbera et al. 2003), Cen X-3 (Suchy et al. 2008), and more recently in GX 301−2 (Suchy et al. 2012), 1A 1118−61 (Suchy et al. 2011; Maitra et al. 2012), and 4U 1626−67 (Iwakiri et al. 2012). We have obtained detailed results on the variation of both the CRSFs of Vela X-1 with the pulse phase. Both the "highecut" and "CompTT" models used by us to fit the spectra give comparable results. This gives us more confidence in the obtained pattern of variation. The results are also very similar to those obtained by Kreykenbohm et al. (2002) with *RXTE* but they did not have enough sensitivity to probe these variations in detail. There have also been attempts to model the CRSF features analytically by assuming certain physics and geometry of the line-forming region by Araya & Harding (1999), Araya-Góchez & Harding (2000), and Schönherr et al. (2007), and more recently by Nishimura (2008, 2011) and Mukherjee & Bhattacharya (2012). All these models predict significant variations in the depth, width, and the centroid energy of the CRSF features with the changing viewing angle at different pulse phases. They also predict possible deviation or distortion from the simple dipole geometry of the magnetic field, and deviation of the line ratios from the classical value of two. Vela X-1 has a shallow and narrow fundamental, and a deep and wide harmonic (refer to Table 1). This may happen due to photon spawning by Raman scattering at higher harmonics (see Schönherr et al. 2007), or the superposition of a large number of lines from different sites in the line-forming region (Nishimura 2008, 2011) may also make the fundamental CRSF appear shallower. Nishimura (2011) further predicts that a shallow and narrow fundamental and a deeper and wider second harmonic would imply large viewing angle w.r.t. the magnetic field. A fan-like beam would be expected for Vela X-1 in this case. As is mentioned in Section 4.2.1 the ratio of the two line energies is >2 at many phases. According to Nishimura (2011), this would favor a line-forming region with a large polar cap or of a greater height. The

fundamental would be formed at a higher site and second harmonic primarily around the bottom. As a result $E2_{\mathrm{cycl}}/E1_{\mathrm{cycl}} > 2$ is expected.

The electron temperature "kT" is high at the phases corresponding to the wider CRSFs, especially at the ascending edges of the high-energy PIN pulse peaks. For a Maxwell–Boltzmann distribution of electrons the observed CRSF FWHM is given as (Mészáros 1992) $W_c \propto E_C \sqrt{kT_e} |\cos\theta|$, where kT_e is the electron temperature, E_C is the CRSF energy, and $\cos\theta$ is the viewing angle w.r.t. the magnetic field. This implies a higher kT_e would result in a higher W_c as is obtained. The fundamental line is deepest at the ascending edge of the pulse phase. The deepest second harmonic is also in the descending edge of the main pulse and very shallow outside the pulses. Nishimura (2011) predicts that these signatures would imply looking at a very large viewing angle w.r.t. the magnetic field at those phases and hence a fan beam-like emission pattern would be expected. All these are however assuming the contribution from one of the magnetic poles of the neutron star, and results may be complicated further with the contribution from the other pole.

REFERENCES

Araya, R. A., & Harding, A. K. 1999, ApJ, 517, 334
Araya-Góchez, R. A., & Harding, A. K. 2000, ApJ, 544, 1067
Bildsten, L., Chakrabarty, D., Chiu, J., et al. 1997, ApJS, 113, 367
Brucato, R. J., & Kristian, J. 1972, ApJL, 173, 105
Choi, C. S., Dotani, T., Day, C. S. R., & Nagase, F. 1996, ApJ, 471, 447
Corbet, R. H. D., & Peele, A. G. 2000, ApJL, 530, 33
Devasia, J., James, M., Paul, B., & Indulekha, K. 2011a, MNRAS, 414, 1023
Devasia, J., James, M., Paul, B., & Indulekha, K. 2011b, MNRAS, 417, 348
Doroshenko, V., Santangelo, A., & Suleimanov, V. 2011, A&A, 529, A52
Doty, J. P., Lewin, W. H. G., & Hoffman, J. A. 1981, ApJ, 243, 257
Enoto, T., Makishima, K., Terada, Y., et al. 2008, PASJ, 60, 57
Fürst, F., Kreykenbohm, I., Pottschmidt, K., et al. 2010, A&A, 519, A37
Galloway, D. K., Giles, A. B., Wu, K., & Greenhill, J. G. 2001, MNRAS, 325, 419
Haberl, F., & White, N. E. 1990, ApJ, 361, 225
Heindl, W. A., Coburn, W., Gruber, D. E., et al. 2000, in AIP Conf. Ser. 510, The Fifth Compton Symposium, ed. M. L. McConnell & J. M. Ryan (Melville, NY: AIP), 173
Inoue, H., Ogawara, Y., Waki, I., et al. 1984, PASJ, 36, 709
Iwakiri, W. B., Terada, Y., Mihara, T., et al. 2012, ApJ, 751, 35
Johnston, M., Bradt, H., Doxsey, R., et al. 1978, ApJL, 223, 71

Kendziorra, E., Mony, B., Kretschmar, P., et al. 1992, in Frontiers Science Series, Proc. Yamada Conference XXVIII, ed. Y. Tanaka & K. Koyama (Tokyo: Universal Academy Press), 51
Klochkov, D., Staubert, R., Postnov, K., et al. 2008, A&A, 482, 907
Koh, D. T., Bildsten, L., Chakrabarty, D., et al. 1997, ApJ, 479, 933
Koyama, K., Tsunemi, H., Dotani, T., et al. 2007, PASJ, 59, 23
Kretschmar, P., Pan, H. C., Kendziorra, E., et al. 1997, A&A, 325, 623
Kreykenbohm, I., Coburn, W., Wilms, J., et al. 2002, A&A, 395, 129
Kreykenbohm, I., Kretschmar, P., Wilms, J., et al. 1999, A&A, 341, 141
Kreykenbohm, I., Wilms, J., Kretschmar, P., et al. 2008, A&A, 492, 511
La Barbera, A., Santangelo, A., Orlandini, M., & Segreto, A. 2003, A&A, 400, 993
Maitra, C., Paul, B., & Naik, S. 2012, MNRAS, 420, 2307
Makishima, K., & Mihara, T. 1992, in Frontiers Science Series, Proc. Yamada Conference XXVIII, ed. Y. Tanaka & K. Koyama (Tokyo: Universal Academy Press), 23
Mészáros, P. (ed.) 1992, High-energy Radiation from Magnetized Neutron Stars (Chicago, IL: Univ. Chicago Press), 544
Mihara, T. 1995, PhD thesis, Univ. Tokyo
Mitsuda, K., Bautz, M., Inoue, H., et al. 2007, PASJ, 59, 1
Mukherjee, D., & Bhattacharya, D. 2012, MNRAS, 420, 720
Nagase, F. 1989, PASJ, 41, 1
Nagase, F., Hayakawa, S., Sato, N., Masai, K., & Inoue, H. 1986, PASJ, 38, 547
Naik, S., Callanan, P. J., Paul, B., & Dotani, T. 2006, ApJ, 647, 1293
Naik, S., Paul, B., Kachhara, C., & Vadawale, S. V. 2011, MNRAS, 413, 241
Nakajima, M., Mihara, T., & Makishima, K. 2010, ApJ, 710, 1755
Nishimura, O. 2008, ApJ, 672, 1127
Nishimura, O. 2011, ApJ, 730, 106
Orlandini, M., dal Fiume, D., Frontera, F., et al. 1998, A&A, 332, 121
Paul, B., Agrawal, P. C., Mukerjee, K., et al. 2001, A&A, 370, 529
Pravdo, S. H., Becker, R. H., Saba, J. R., & Serlemitsos, P. J. 1977, IAU Circ., 3116, 2
Pravdo, S. H., Bussard, R. W., Becker, R. H., et al. 1978, ApJ, 225, 988
Quaintrell, H., Norton, A. J., Ash, T. D. C., et al. 2003, A&A, 401, 313
Rawls, M. L., Orosz, J. A., McClintock, J. E., et al. 2011, ApJ, 730, 25
Robba, N. R., Burderi, L., Di Salvo, T., Iaria, R., & Cusumano, G. 2001, ApJ, 562, 950
Rose, L. A., Marshall, F. E., Holt, S. S., et al. 1979, ApJ, 231, 919
Rybicki, G. B., & Lightman, A. P. (ed.) 1986, Radiative Processes in Astrophysics (New York: Wiley), 400
Sako, M., Liedahl, D. A., Kahn, S. M., & Paerels, F. 1999, ApJ, 525, 921
Schönherr, G., Wilms, J., Kretschmar, P., et al. 2007, A&A, 472, 353
Soong, Y., Gruber, D. E., Peterson, L. E., & Rothschild, R. E. 1990, ApJ, 348, 641
Suchy, S., Fürst, F., Pottschmidt, K., et al. 2012, ApJ, 745, 124
Suchy, S., Pottschmidt, K., Rothschild, R. E., et al. 2011, ApJ, 733, 15
Suchy, S., Pottschmidt, K., Wilms, J., et al. 2008, ApJ, 675, 1487
Takahashi, T., Abe, K., Endo, M., et al. 2007, PASJ, 59, 35
Tanaka, Y. 1986, in IAU Colloq. 89, Radiation Hydrodynamics in Stars and Compact Objects, ed. D. Mihalas & K.-H. A. Winkler (Lecture Notes in Physics, Vol. 255; Berlin: Springer), 198
Titarchuk, L. 1994, ApJ, 434, 570
van Kerkwijk, M. H., van Paradijs, J., Zuiderwijk, E. J., et al. 1995, A&A, 303, 483
Watanabe, S., Sako, M., Ishida, M., et al. 2006, ApJ, 651, 421
White, N. E., Swank, J. H., & Holt, S. S. 1983, ApJ, 270, 711